Contactless control of suspended loads for offshore installations
Proof of concept using magnetic interaction

Atzampou, Panagiota; Meijers, Peter C.; Tsouvalas, Apostolos; Metrikine, Andrei V.

DOI
10.1016/j.jsv.2024.118246

Publication date
2024

Document Version
Final published version

Published in
Journal of Sound and Vibration

Citation (APA)
Atzampou, P., Meijers, P. C., Tsouvalas, A., & Metrikine, A. V. (2024). Contactless control of suspended loads for offshore installations: Proof of concept using magnetic interaction. *Journal of Sound and Vibration*, *575*, Article 118246. https://doi.org/10.1016/j.jsv.2024.118246

Journal of Sound and Vibration 575 (2024) 118246

Contents lists available at ScienceDirect

Journal of Sound and Vibration

journal homepage: www.elsevier.com/locate/jsvi

Contactless control of suspended loads for offshore installations: Proof of concept using magnetic interaction

Panagiota Atzampou *, Peter C. Meijers, Apostolos Tsouvalas, Andrei V. Metrikine

Civil Engineering and Geosciences, Delft University of Technology, Stevinweg 1, Delft, 2628CN, Netherlands

ARTICLE INFO

Keywords:
Contactless control
Magnetic pendulum
PID control
Active vibration control
Motion manipulation
Offshore wind installation

ABSTRACT

Current offshore wind turbine installation and positioning methods require mechanical equipment attached on the lifted components and human intervention. The present paper studies the development of a contactless motion compensation technique by investigating a magnetically controlled pendulum. The technique involves the interaction of a magnetic pendulum with an electromagnetic actuator. Two control modes are considered: the imposition of a desired motion to the mass and the motion attenuation of a prescribed pivot excitation. The numerical model is validated and calibrated against experiments and demonstrates excellent predictive capabilities. The control exerted is effective for a broad range of excitation frequencies and amplitudes. Important parameters associated with the performance of the technique such as the separation distance of the magnets and the saturation of the controller are identified. The controllability regions for effective control depending on the characteristics of the excitation are derived. The force amplitude of the contactless actuator is comparable to currently-used active tugger line control systems, but with the additional advantage of both attractive and repulsive forces. The findings of this paper illuminate the path for the further development of a non-contact control technique which has the potential to increase the efficiency of offshore wind installations.

1. Introduction

Offshore wind is one of the most promising and formidable renewable energy sectors at present [1]. Offshore wind turbines (OWT) are designed with larger dimensions and can be installed by floating heavy lift vessels (HLV) in deep waters to comply with the ever increasing demand for energy generated from renewable sources. This type of floating installations is subject to loads caused by the action of wind and waves, which consequently introduce external disturbance to the crane-payload system hindering the efficiency of the OWT installation [2].

A plethora of motion compensation and position control techniques has been employed during the installation operations (in order to subdue the disturbances) and has been thoroughly tested *in situ* over the years. For bottom-founded OWT installations, fixed and motion compensating gripper frames are widely employed [3]. Further motion attenuation techniques to maintain the correct position of the hanging load have been investigated. One of these techniques is either the use of manually manipulated tugger lines attached to the component or active tugger line motion control systems [4], which exert merely attractive forces by requiring a constant tension force present in the tuggers. Alternatively, the motion compensation of the payload has also been introduced indirectly by means of motion control of the crane itself. These methods frequently pertain to the attenuation of the vessel motions through a motion compensated platform [5], crane cart motion manipulation [6] and crane parameter modification to minimize payload pendulation [7]. Other techniques involve active and passive crane heave compensation [8]. However, the aforementioned

* Corresponding author.
E-mail address: p.atzampou@tudelft.nl (P. Atzampou).

https://doi.org/10.1016/j.jsv.2024.118246
Received 7 August 2023; Received in revised form 28 December 2023; Accepted 4 January 2024
Available online 5 January 2024

methods require either mechanical equipment in direct contact with the target payload or active human intervention. These facts, amplified by the delicate nature of positioning OWT components, the small error tolerances and the harsh offshore environment, illuminate a gap in research for a direct but non-contact position control technique of OWT installations. Such a technique would both contribute to the safety of the crew (by reducing the risk associated with human interventions offshore) and positively influence the duration of the overall procedure, a major deciding factor for the efficiency and cost of the operation. This concept utilizes magnetic forces, a relatively new practice in the field of structural engineering, especially given the large scale of the intended application.

In this paper, the dynamical system concerns a single-degree-of-freedom (1DOF) magnetic pendulum interacting with an electromagnetic actuator. This magneto-mechanical analogue serves as a proof of concept for the envisioned contactless technique and resembles a simplified version of a suspended OWT component during the installation. The system consists of a (point mass) pendulum with a permanent magnet attached on its mass. The pendulum is excited by the kinetically prescribed motion of its pivot and the action of an electromagnet.

Literature abounds with research involving the interaction of magnetically excited pendula and the chaotic and non-linear phenomena they introduce. First, they can function as structural vibration damping devices, e.g. passive [9,10] and active [11] energy absorbers. Second, chaotic pendula or externally-excited pendula can contribute to energy harvesting through their oscillations [12,13]. Regarding the set-up of the dynamical systems, work has been conducted for magnetic pendula with a permanent magnet mounted to the suspended mass and either a permanent magnet [14] or an electromagnet (solenoid or coil) below the pendulum's equilibrium point [15,16]. In the latter configuration, a pulsating current signal (repulsing [17] or attractive) is introduced to excite the system. In the present work, the set-up and orientation of the two magnets differ from previous studies as the actuator is located in line with the mass of the pendulum (instead of above its equilibrium), while the magnetic interaction utilizes alternating polarities (both attraction and repulsion cycles) as means-to-an-end for the motion control of the pendulum. Moreover, experimental measurements are compared to numerical simulations to assess the ability of predicting and validating the response of such an inherently non-linear interaction.

In terms of control, the number of studies on magnetically controlled pendula is rather scarce. Ranging from a simple control (using switch on and off conditions) of an attracting magnetic field of a solenoid as external excitation of a mass-pendulum system model [18] to a control technique based on the width of the applied pulse and position sensing of a pendulum [19]. Ida [19] studied a magnetic pendulum of an embedded magnet on the mass and a pulsing coil that repelled the mass at the equilibrium position and attracted it, at the maximum amplitude of oscillation. Fradkov et al. [20] developed a pulse-modulated control law for the excitation and oscillation synchronization of a mechatronic system of two coupled double pendulums via the speed-gradient method. Kraftmakher [21] designed a magnetically controlled compound pendulum with two permanent magnets mounted into each free tip and two adjacent electromagnets on both sides. The upper magnet received the excitation and the interaction of the magnets on the other end served as a damping restoring torque. While these studies aimed for a limited or fixed position for the pendulum, the opportunity for a time variant motion manipulation is highlighted. During the installation of an OWT tower by a floating vessel (Fig. 1), the target of the installation (e.g. pre-installed monopile) moves with respect to the vessel-crane-load system. This motion is a result of the action of wind and waves on both the vessel and the installation target. Thus, a controller that imposes a desirable motion to the hanging load (e.g. the OWT tower) such that it negates the relative motion between the target of installation and the load is worth investigating.

The present study introduces and investigates the efficient (low error without exceeding the actuator's capacity) position control of the pendulum's motion. The position control concerns two separate modes. The first mode deals with the imposition of a certain time-varying motion pattern on the hanging load with a stationary suspension. This motion pattern acts as a desired response of the dynamic system, simulating the relative motion of the target and the mass-crane-vessel system offshore. This control mode is validated and compared against experimental data to prove the predictive abilities of the numerical model. The second control mode involves the attenuation of the external disturbances (e.g. crane tip motions) aiming at maintaining a fixed desired position. To study these control cases, a modified PD controller is employed.

The paper is structured as follows: Section 2 describes the dynamical system and experimental set-up, while Section 3 presents the parametric calibration of the numerical model against the experiments for the non-linear electromagnetic and damping forces. In Section 4, the development of the modified PD control is elaborated. Section 5 reports the results and the corresponding remarks for the different cases of controlled vibrations studied. Finally, Section 6 presents the main conclusions drawn.

2. Dynamical system

2.1. Description of the dynamical system

A typical dynamical system during an offshore operation is presented in Fig. 1 and consists of a (floating) semi-submersible vessel, a crane-payload (suspended tower) system and a desired target position of installation (monopile head). The contactless control method envisioned is based on the magnetic interaction of an electromagnetic actuator and a permanent magnet located on the suspended payload.

In order to create the base case for the proof of concept of the control technique, the aforementioned system was simplified. More specifically, the set-up consists of an immobile crane-shaped frame (representing the offshore crane), an inflexible aluminium rod that serves as the arm of the pendulum (equivalent to the crane cable and hook) and an aluminium solid cube for the pendulum mass (analogue to the OWT suspended payload). The hanging load is modelled as a point mass, restrained to oscillate in one plane; thus, the apparatus resembles the problem of a single degree-of-freedom (SDOF) simple pendulum. The wave-induced vibrations of

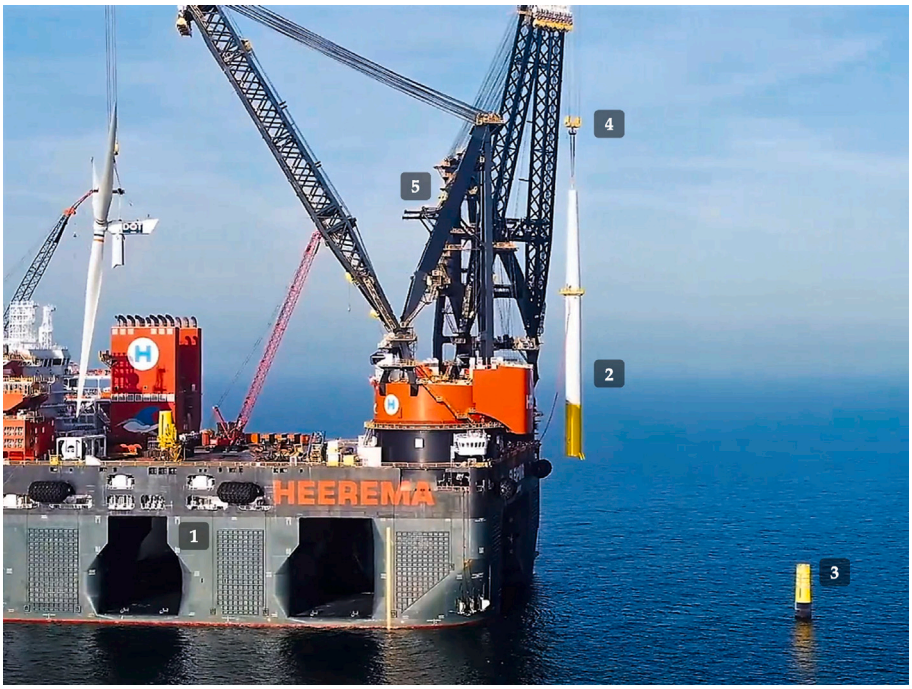

Fig. 1. Semi-submersible crane vessel (HMC-Sleipnir) performing a floating offshore installation of an OWT tower: 1. Floating vessel, 2. Offshore wind turbine tower, 3. Monopile head, 4. Crane hook load and cable, 5. Heavy lift crane [22].

the floating vessel-crane system are translated as external excitation through the motion of the pivot point of the pendulum. The same set-up was considered for both experimental (Fig. 2(a)) and numerical simulations (Fig. 2(b)).

The actuation of the system comprises a holding electromagnet (*Eclipse Magnetics* EM65-24V-DC) at a constant initial distance from the target suspended load. In order to achieve both attraction and repulsion conditions for the oscillations, a neodymium permanent magnet (N52 Ø15x3 mm) (PM) is attached and positioned at the centre of the side of the cube parallel to the electromagnet (EM) as presented in the detail in Fig. 2(a). The dipole moment of the PM is aligned with the EM.

Regarding the components of the experimental apparatus, a USB development board (Teensy 3.6) is utilized as a microcontroller for the control algorithm, while the data are logged using data acquisition software developed in-house by the technicians of Stevinlab II (TUDelft). Moreover, the software enables for the real-time modification of the control parameters, whereas the time series of the measured output and input signal of the electromagnet as well as the control variable are recorded with a sampling rate of 20 Hz.

For the regulation of the voltage input of the electromagnet, an H-bridge electronic circuit is employed, whereas the power supply box has indicators for the voltage and intensity of the electricity generated. Lastly, for the purpose of tracking and logging the pendulation of the point mass, a laser distance measuring device is employed (*Altheris* FDRD603-100) with the sampling rate of 20 Hz. The pointer of the laser is aimed at the centre of the hanging mass and the displacement from its equilibrium position is measured with the positive horizontal axis facing the EM as shown in Fig. 2(b) as positive x-axis orientation.

The development of the magnetic field exerted by the electromagnet is measured through a Hall-effect magnetic field sensor (*Honeywell* SS491). Fig. 3 presents the schematic placement of the sensor (8 mm from the edge). The sensor measures one of the components of the magnetic field ($\vec{B}$), while the orientation of the sensor is calibrated such that $\vec{H}$ has the same positive direction as the $\vec{B}$ field generated by the EM by a positive voltage.

2.2. Governing equations

The dynamical system consists of a simple pendulum with a mass M connected to a rigid rod of total mass m rotating around the pivot point. The pendulum is subjected to external excitation $F(t)$ imposed by the EM and a horizontal prescribed motion of the pivot point $h(t)$. The configuration is presented schematically in Fig. 2(b) and shows the global fixed axes (x_G, y_G) and the moving with the pivot axes (x, y) of the system as well as the positive assumed directions for the angular (θ) and linear (u, u_n) displacements. Due to the moving point of rotation, the motion of the mass of the pendulum is characterized by two horizontal displacements; one from the equilibrium position given by u (the unknown state of the system) and one derived from the global reference system $u_n = u + h$. The initial distance d and the time-variant separation distance $s = d - u_n$ between the EM and PM are defined in Fig. 2(b). Table 1 demonstrates quantitatively important parameters of the set-up.

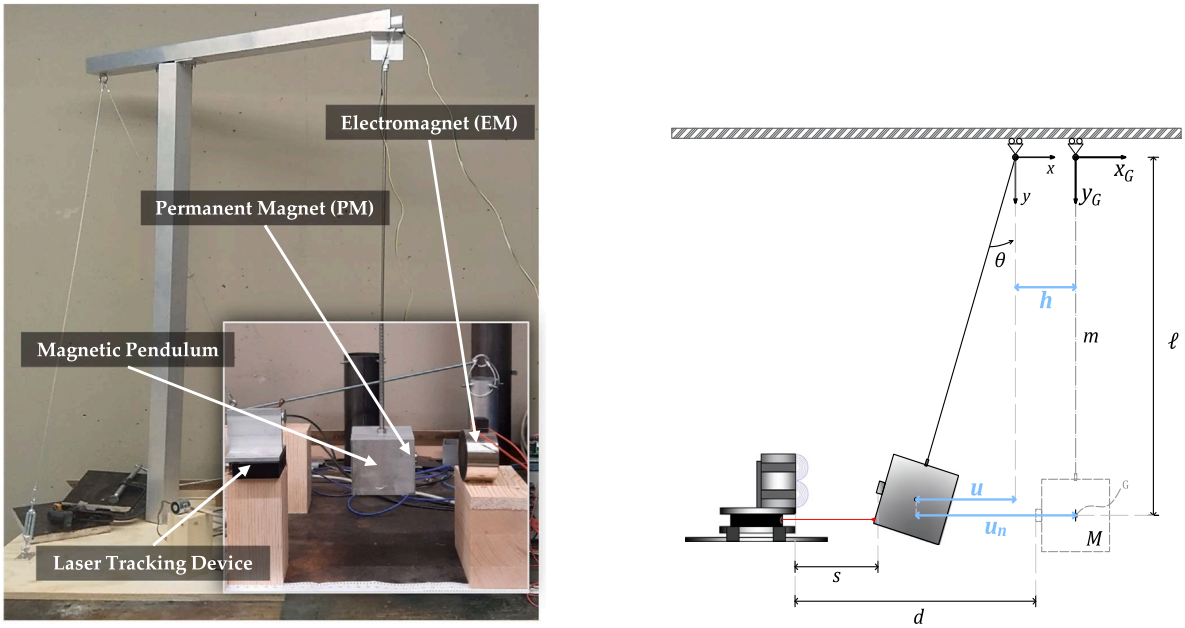

Fig. 2. (a) Annotated photograph of the physical model. (b) Schematization of the numerically simulated pendulum with a moving pivot point.

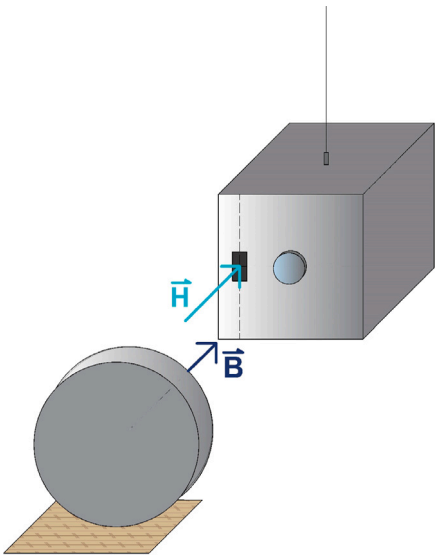

Fig. 3. Hall sensor placement and orientation.

Table 1
Set-up dimensions.

ℓ [m]	M [kg]	m [kg]	Cube Size [mm]	PM Size [mm]	EM Size [mm]
1.04	0.9382	0.1868	70 x 70 x 70	Diameter = 15 Thickness = 3	Diameter = 65 Thickness = 35

The equation of motion (EOM) of the single degree-of-freedom (SDOF) system reads:

$$\left(M+\frac{m}{3}\right)\ell^2\ddot{\theta}+\left(M+\frac{m}{2}\right)g\ell\sin(\theta)=-\left(M+\frac{m}{2}\right)\ell\ddot{h}+\Sigma T, \tag{1}$$

where θ describes the angle of pendulation, and it is a function of time, while m and M represent the mass of the rod and the suspended load respectively. The length of the arm of the pendulum is given by ℓ. The gravitational acceleration g is equal to $9.81\,\mathrm{m/s^2}$. On the right hand side of Eq. (1), ΣT corresponds to the summation of the external non-conservative torques acting on the pendulum. In the present study, these torques are a result of the action of the damping force (D) present at the pivot point hinge and the electromagnetic interaction (F) force between the two magnets. It is noted that the torque which would be generated due to the aerodynamic forces is not considered as an additional external disturbance for this initial investigation due to limitations of the physical experimental set-up. These forces are not expected to have significant influence on the control outcome as the pivot point motion is the dominant external excitation of the system. A detailed description of the derivation of the EOM of the present system can be found in the Appendix A.

In order to simplify the simulation of the system the following assumptions are made: 1) The arm of the pendulum is an inextensible rod restraining the mass to oscillate in-plane; 2) the displacement of the mass is small compared to the length of the pendulum, resulting in the small angle approximation being assumed ($\sin\theta\approx\theta$). Therefore, the unknown degree of freedom of the system corresponds to the translation of the mass in the horizontal axis, i.e. $u=\ell\theta$. The linearized EOM is given by

$$\left(M+\frac{m}{3}\right)\ddot{u}+\left(M+\frac{m}{2}\right)\frac{g}{\ell}u=-\left(M+\frac{m}{2}\right)\ddot{h}+F+D, \tag{2}$$

where the dot above a variable denotes a derivative with respect to time. The undamped natural frequency (ω_n) of the dynamical system amounts to

$$\omega_n=\sqrt{\frac{M+\frac{m}{2}}{M+\frac{m}{3}}\frac{g}{\ell}}\approx 3.12\,\mathrm{rad/s},\quad\text{and}\quad f_n=\frac{\omega_n}{2\pi}\approx 0.496\,\mathrm{Hz} \tag{3}$$

where the numerical values in Table 1 are considered.

3. Parametric calibration

3.1. Damping force

The metal hinge-type suspension pivot point for the rod of pendulum introduces a source of dissipation of energy for the system. This dissipation, in the numerical simulations, is accounted for as an active external force acting on the suspended mass. This damping force is described by Coulomb's friction formula and has the following form [23],

$$D=\frac{M_{fr}}{\ell}=-\mu\,\mathrm{sign}\,(\dot{u}), \tag{4}$$

where M_{fr} is the frictional moment at the hinge and μ corresponds to the kinetic friction.

Coulomb friction is a non-linear dissipative force and its action depends on various factors [24]. These factors pertain to the state (lubricated or dry) of the system and the relative time and temperature of the measurement, as well as the frequency and amplitude of the oscillation. In addition, kinetic friction introduces memory effects, namely friction may change during the oscillation itself. The simulation of friction with high accuracy is a tedious stand-alone task and involves experiments with little reproducibility [24]. Additionally, such a damping force results from the specific experimental mechanical components (i.e. the hinge-type connection), and it is not an important feature of the real applications offshore. Hence, the dissipative force given by Eq. (4) will be used in this work, as it is the simplest model that can sufficiently emulate the observed behaviour of the system.

Free vibrations can be used as control scenarios, where important system parameters are identified quantitatively. The damping force of the numerical simulations is calibrated against experimental data. Fig. 4 demonstrates a typical damped vibration measured in the lab for two cases of initial positions. The time trace of the motion display an evident linear decay of the damped oscillation. Such a linear envelope indicates the presence of Coulomb's friction in the system [23].

The calibration of the damping coefficients was performed by releasing the pendulum mass from different initial positions ($u\,(0)\in[10,50]$ mm) and recording the response. The free vibration time series was compared to the corresponding signal provided by the numerical simulation, while the coefficients were tuned using a grey box non-linear system identification algorithm in MATLAB, and the empirical trial and error method. Three iterations of free vibrations for each initial position were performed and the mean values are deduced to obtain better representative constants. Further validation is provided by the formula derived by Torzo and Peranzoni [23] for the case of a simple pendulum under sliding friction given by

$$\mu=\Delta\theta\frac{M\ell g}{2}, \tag{5}$$

where $\Delta\theta$ represents the slope of the linear envelope of the decay in units rad/s, M and ℓ the mass and the length of the pendulum respectively and g the gravitational acceleration. The value of $\Delta\theta$ is extracted from the coefficient of the linear approximation of the linear decay envelope. The calibration of the friction yields the constant value $\mu=0.005\,\mathrm{kg\ m/s^2}$. The overall convergence ratio between the model prediction and the actual measurement is derived as $fit(\%)=(1-\kappa)$, where κ represents the normalized root mean square error (NRMSE) and amounts up to 80% and 50% for $u(0)=50$ mm and 20 mm respectively. This difference in efficiency is

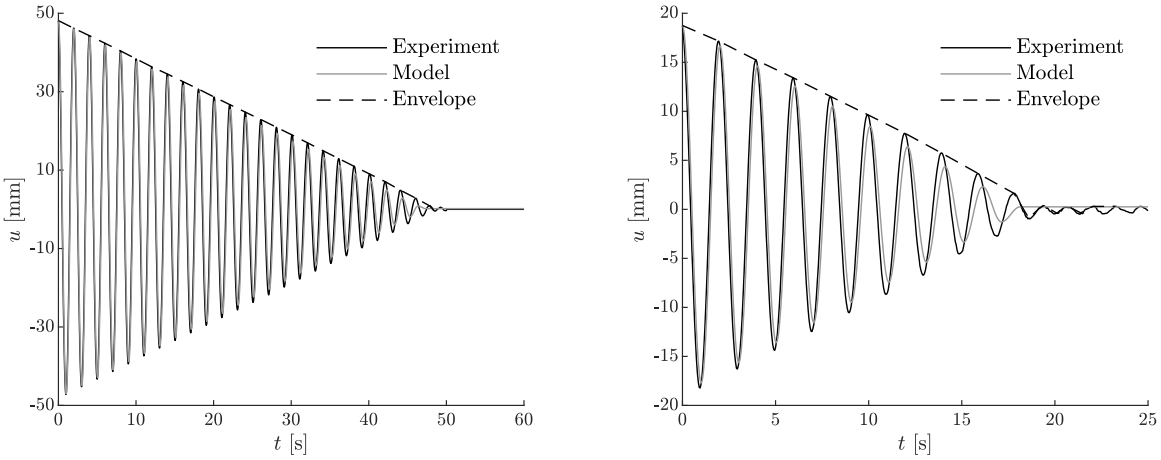

(a) $u(0) = 50\,\text{mm}$ (b) $u(0) = 20\,\text{mm}$

Fig. 4. Damping calibration of numerical simulations against experimental data for different initial distances $u(0)$.

evident in Fig. 4(b) where the simulations predict a slightly more damped response in terms of amplitude and a misfit in phase as the motion approaches zero amplitude. Moreover, the small amplitude oscillations around the equilibrium point observed in the experimental data are not captured by the model. Nonetheless, simulations using the simple Coulomb friction model give satisfactory results compared to the measurements (Fig. 4(a)). It is expected that, for the controlled vibrations, the exact representation of the damping is not critical in obtaining the desired result due to the compensation of the PD controller provided that oscillations are not of extremely low amplitude.

3.2. Electromagnetic force

The external excitation acting upon the pendulum results from the interaction between two magnets; one magnet of fixed polarity and strength (PM) and one electromagnet (EM). A series of experimental data was collected to derive a function to represent this interaction. More specifically, the electromagnet was set in different initial distances from the pendulum mass while both cycles of attraction and repulsion were investigated. In this section, the derivation and validation of the empirical experimentally-derived formula is shown. Assuming that the PM can be approximated by a magnetic dipole $\vec{m}$, the force $\vec{F}$ on the PM (resulting from the magnetic interaction with the EM) is given by the gradient of the magnetic energy [25]:

$$\vec{F} = \nabla\left(\vec{m}\cdot\vec{B}\right), \tag{6}$$

in which ∇ represents the gradient operator, $\vec{m}$ is the dipole moment of the PM, and $\vec{B}$ is the magnetic field of the EM at the location of the PM. Assuming that the displacement of the pendulum is small compared to its length, the motion is restricted to the x-axis. Furthermore, the dipole moment $\vec{m}$ is assumed to be aligned with the x-axis. Hence, only the force component along this axis is relevant for the dynamics of the system. Using these assumptions, the force F is given by

$$F = \frac{d}{dx}\left(m_x B_x\right), \tag{7}$$

in which m_x is a time and space invariant constant representing the unknown strength of the PM. Given the relatively complex geometry of the EM, creating a model for the magnetic field B_x is not a trivial task. Therefore, the spatial variation of the field is determined from measured data. Fig. 5 presents the magnetic field measured by the Hall sensor for different separation distances s, where $s = d - u$. A fit to the data for three distinct values of supply voltage V (Fig. 5) shows that the field can be modelled as follows:

$$B_x = \frac{\alpha' I}{s^2}, \tag{8}$$

in which I denotes the current in the coil of the magnet, which is directly proportional to the static voltage via $V = RI$. Note that, in the above, the electrical resistance R of the coil is merged into the fitting parameter α'. Substituting the magnetic field into the force expression yields

$$F = \frac{d}{dx}\left(m_x \frac{\alpha' I}{s^2}\right) = 2m_x \frac{\alpha' I}{s^3} = \frac{\alpha J}{s^3} = \frac{\alpha J}{(d-u)^3}, \tag{9}$$

in which $J = RI$, and α is a model constant accounting for the strength of the PM, the strength and geometry of the EM. The tolerances that accompany Eq. (9) pertain to the minimum and maximum marginal initial relative distance, where the formula

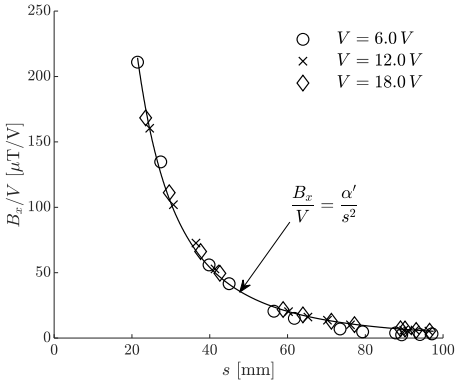

Fig. 5. Determination of the dependency of the magnetic field generated by the EM with distance and applied voltage.

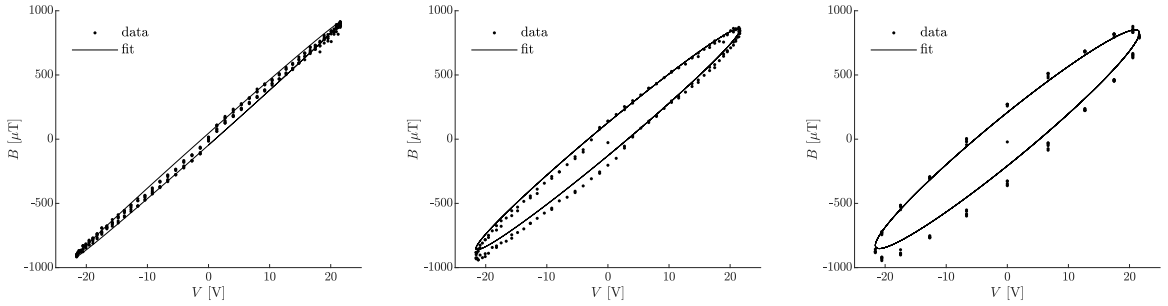

(a) 0.2 Hz (b) 0.6 Hz (c) 1.0 Hz

Fig. 6. Determination of the time constant τ of the RL circuit.

is efficiently representative of the non-linear phenomenon. This distance range translates to $d \in [25, 75]$ mm. Fig. 5 shows the comparison between the experimental data set and the mathematical approximation formula.

As a result of self-inductance L of the magnet, the current in the EM will not be proportional the supplied voltage $V(t)$. To account for this effect, the current in the EM is modelled as an elementary RL circuit [26]:

$$\dot{J} = \frac{1}{\tau}(V(t) - J), \tag{10}$$

where the derivative of the voltage output with respect to time is given by $\dot{J}$ with $J = RI$ and $\tau = L/R$. Since the numerical value for resistance R of the circuit can be condensed into the model coefficient for the magnetic field, the response of the circuit is fully determined by the time constant τ. The numerical value of the latter is easily extracted from measurement data, in which the magnetic field is determined for various harmonic voltage signals (Fig. 6). By fitting the solution of the RL circuit model, it follows that $\tau = 0.040\,\mathrm{s}$.

Now the general equation for the magnetic interaction force is known, the coefficient α is to be determined. For this, the equilibrium position u_0 of the pendulum is measured for different constant values of the supply voltage. For static conditions, all time derivatives vanish from Eq. (2) and the following relation applies:

$$\left(M + \frac{m}{2}\right)\frac{g}{\ell}u_0 = \frac{\alpha J}{\left(s - u_0\right)^3}, \tag{11}$$

For an initial separation distance of $d = 50\,\mathrm{mm}$, Fig. 7 presents the measured values for the equilibrium position. By fitting Eq. (11) to this data, it is found that $\alpha = 2.5810 \times 10^{-7}\,\mathrm{Nm^3/V}$.

4. PD control

To control the motion of the pendulum via the intensity of the electromagnetic interaction, a PID controller is employed. The basic equation of a PID controller in time domain [27] is given by

$$c(t) = K_p\, e(t) + K_i \int e(t)dt + K_d\, \dot{e}(t), \text{with } e(t) = \xi(t) - u_n(t) = [\xi(t) - h(t)] - u(t), \tag{12}$$

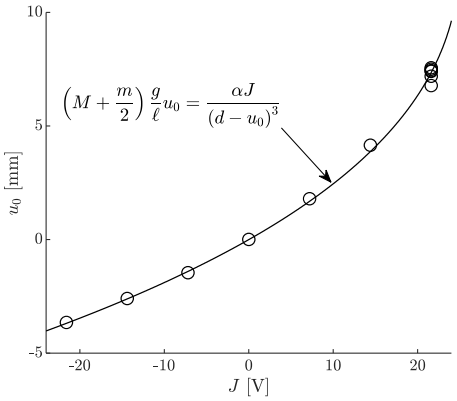

Fig. 7. Measurements of the static equilibrium position of the pendulum with $d = 50\,\text{mm}$ for different supply voltages, and a fit to data to determine the magnetic interaction coefficient.

where $c(t)$ is the control variable, i.e. the voltage input of the electromagnet $V(t)$, and K_p, K_i, K_d represent the proportional, integral and derivative gains of the PID controller respectively. The error term $e(t)$ captures the divergence of the current measured systems output $u(t)$ and the desired position $\xi(t)$.

Given the application, the desired position can be a time-varying function, consisting of a sum of different harmonic signals. Therefore, it is expected that the integral term of the PID control will not have a considerable influence on to the output of the controller, as the overshoot produced by the K_i contribution will be followed by an undershoot and on average leading to a negligible contribution. The same holds for the case of disturbance rejection at a fixed position, when this position refers to the equilibrium, $\xi(t) = 0$. In this control case, the additional damping force provided by the derivative term of the controller is most decisive for a good control performance. As a result, only the proportional and derivative components of the control output are considered, essentially performing PD control.

The system under consideration is subjected to a non-linear forcing, which, in this case, functions as the means for control. A potential linearization of the electromagnetic force around the static equilibrium of the pendulum is unlikely to be fruitful, since such an approximation would significantly decrease the range of applicability (the horizontal displacement bandwidth where the model for the electromagnetic force is still a reasonable approximation of the interaction force). Thus, in order to linearize the problem without taking a toll on the accuracy and representation of the electromagnetic interaction, an additional path is included into the control algorithm. This path, which bears a similarity to the non-linear control techniques of feedback linearization [28] or gain scheduling [28], is employed for the sole purpose of replacing the current non-linear control force with a linear control output for the PD control. More specifically, the control output $c(t)$ is multiplied by a correction factor γ, creating a new control output $c'(t)$, which is now used as the control variable and is given as

$$c'(t) = K'_p(u(t))\, e(t) + K'_d(u(t))\, \dot{e}(t), \tag{13}$$

in which $K'_p(u(t)) = \gamma K_p$, and $K'_d(u(t)) = \gamma K_d$, where $\gamma = s^3/\alpha$. With this modification, the PD gain parameters are converted from constant values to state-dependent coefficients. Due to the physical limits of the actuators performance, the new control output $c'(t)$ bears saturation limits,

$$\text{sat}(c'(t)) = \begin{cases} -24\,\text{V} & \text{if } c'(t) < c'_{\text{limit}^-} = -24\,\text{V}, \\ +24\,\text{V} & \text{if } c'(t) > c'_{\text{limit}^+} = +24\,\text{V}. \end{cases} \tag{14}$$

As previously mentioned, the applied voltage prescribed by the modified PD controller, is not directly proportional to the current intensity in the electromagnet, but rather it is given by Eq. (10).

To summarize the PD controller algorithm, a block diagram of the modified PD control loop is presented in Fig. 8, and the relevant equations of motion are given by:

$$\left(M+\frac{m}{3}\right)\ddot{u} + \left(M+\frac{m}{2}\right)\frac{g}{\ell}u = -\left(M+\frac{m}{2}\right)\ddot{h} + \mu\,\text{sign}\,(\dot{u}) + \frac{\alpha J}{s^3}, \tag{15a}$$

$$\dot{J} = \frac{1}{\tau}(c'(t) - J), \tag{15b}$$

$$c'(t) = \left[K'_p\,(\xi - u_n) + K'_d\,(\dot{\xi} - \dot{u}_n)\right]_{c'_{\text{limit}^-}}^{c'_{\text{limit}^+}}. \tag{15c}$$

Due to the non-linear nature of these equations, the system is studied in the time domain.

5. Results

In this section, two distinct cases of controlled vibrations are considered:

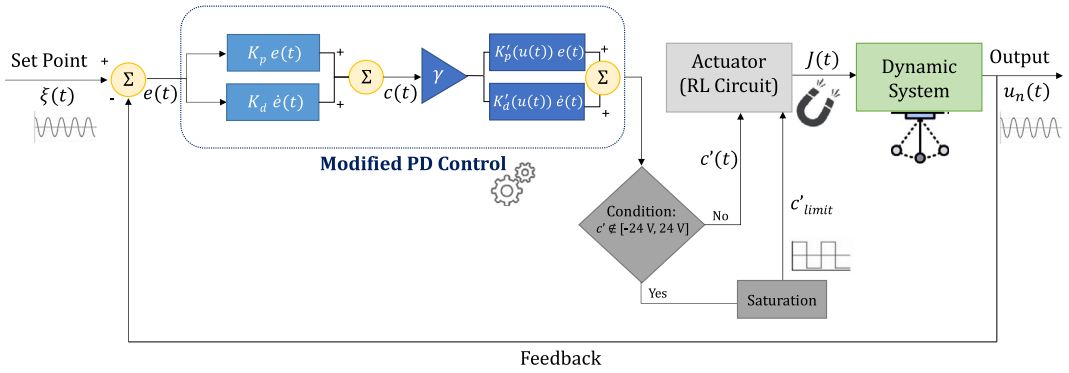

Fig. 8. Block diagram for the modified PD control.

1. *Desired motion control*: Imposition of a desired motion pattern to the suspended mass M;
2. *Disturbance rejection*: Attenuation of the dynamic response of the pendulum mass M when subjected to an external excitation to maintain a desired fixed position.

Moreover, an additional scenario is studied with a more realistic multiple-harmonic suspension point excitation to demonstrate the efficiency of the magnetic manipulation of this simple mass pendulum.

5.1. Desired motion control

In this section, desired motion control is defined as imposing a prescribed motion to the pendulum mass with a stationary pivot point ($h(t) = 0$). This control mode is relevant for floating vessel OWT installations, where the target of the installation (e.g. a monopile) moves relatively to the vessel-crane-load system. This motion results from dynamic disturbances (waves, wind etc.) on the latter system.

The modified PD control algorithm is employed to impose the desired motion pattern to the pendulum: a single-harmonic motion: $\xi(t) = A\sin(\omega t)$. For the activation of the PD control, a set of constant coefficients for the gains K_p and K_d are selected for the simulations. The values of the coefficients are chosen heuristically by means of trial and error and reflected a sufficient level of motion control for the experimental tests. The gains of PD control are equal to $K_p = 631\,\mathrm{N/m}$ and $K_d = 100\,\mathrm{Ns/m}$ respectively.

Given the distance-dependent nature of the electromagnetic force, the most deciding variable in terms of control efficiency was the initial separation distance d. Therefore, in Fig. 9 the displacement time series of the same desired motion pattern ($\omega/\omega_n = 0.6$ and $A = 5\,\mathrm{mm}$) is presented, but for decreasing initial distance. It is evident that the efficiency of the control improves as d decreases, while the convergence of the experimental and modelled data is satisfactory with the discrepancies attributed to noise and disturbances associated with the physical experiment. Moreover, the optimal separation distance for the case presented is $40\,\mathrm{mm}$, as for the smallest separation distance (Fig. 9(c)) the experimental curve appears less smooth. This highlights the importance of accounting for the non-linearity of the force and the fact that an active range of operability should be set for the interaction to occur with the appropriate effectiveness (upper distance limit) and to eliminate unwanted unstable behaviour (lower distance limit).

During the experiment, the internal control variables were not registered, and, as a result, it is not possible to directly assess the error, output and saturation level of the controller. Fortunately, the numerical model has shown to be able to satisfactorily predict the corresponding physical behaviour. Hence, it is sufficient to draw conclusions on the performance of the controller by considering only the results of the numerical simulations.

An important parameter of the efficiency of the control is the deviation of the response from the desired motion, i.e. the error. In order to achieve a better understanding of the correlation of the error with the modifiable variables of the control (in this case the frequency of the desired oscillation), a representative value for the error observed in each excitation scenario is derived. This value is the RMS error (e_{RMS}) and is given by [29] as

$$e_{\mathrm{RMS}} = \sqrt{2}\sqrt{\overline{\left(e(t) - \overline{e(t)}\right)^2}}, \tag{16}$$

where $e(t)$ is the steady-state error of the PD control and $\overline{e(t)}$ the mean value of the error time series. The overbar represents the mean value of the enclosed function and it is given by

$$\overline{f(t)} = \frac{1}{N}\sum_{1}^{N} f(t), \tag{17}$$

where N refers to the total number of data points and $f(t)$ to a generic function.

In any case, the physical limits of the actuation system should not be omitted when the overall performance of the control is assessed. When the error becomes higher, the EM compensates by reaching the full capacity of the applied voltage and thus

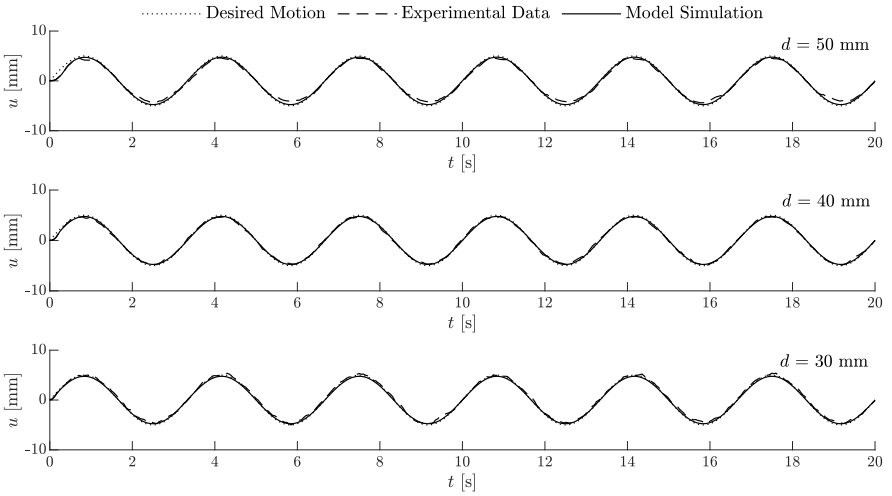

Fig. 9. Displacement time series of controlled motion for harmonic desired motion pattern with different initial separation distances: (a) d = 50 mm, (b) d = 40 mm, (c) d = 30 mm.

saturates. To quantify this saturation, a saturation level indicator (SP) is introduced, which is equal to the percentage of the total time in which the electromagnet functions at the maximum voltage. It is calculated as

$$\mathrm{SP}(\%) = \frac{T_s}{T_{\mathrm{tot}}} \cdot 100\%, \tag{18}$$

where T_{tot} is the total duration of the simulation or experimental test, while T_s refers to the cumulative time in which the supply voltage of the EM is above 95% of the physical limit $\left(|V(t)| > 0.95\ c'_{\mathrm{limit}^{\pm}}\right)$.

Fig. 10(a) and Fig. 10(b) illustrate the error value e_{RMS} and the total saturation SP with respect to the desired frequency of motion and for different initial separation distances. An instantaneous increase of the error is observed at certain frequencies and corresponds well to critical values of the frequency (ω_c) where the controller is abruptly fully saturated. This frequency value differs in the cases studied; the closer the two magnets are located initially, the higher this critical frequency becomes. The critical frequency signifies the cut-off point for an efficient control with the chosen control parameters. In Fig. 10(a), the case of $d = 30$ mm demonstrates a broader frequency range of motion control and a smoother transition from low to higher error values. Moreover, in terms of saturation (Fig. 10(b)), the frequency point of the abrupt change coincides better with the error jump when the separation distance is larger. Hence, this indicated that moving the actuator closer to the mass M increases the frequency range in which the control operates at full capacity, i.e. maintaining a low deviation from the desired motion pattern. For low frequencies ($f < 0.3$ Hz or $\omega/\omega_n < 0.5$) and for the case of $d = 50$ mm, the controller is saturated for a short time span in the simulation while maintaining a low overall error. This effect is eliminated when the distance between the two magnets is reduced. In short, the control is effective: 1) for $d = 50$ mm, when $0 \leq \omega/\omega_n \leq 1.30$, 2) for $d = 40$ mm, when $0 \leq \omega/\omega_n \leq 1.60$ and 3) for $d = 30$ mm, when $0 \leq \omega/\omega_n \leq 2.05$. The non-proportional relation of the distance and the critical frequency is indicative of the non-linear nature of the electromagnetic interaction. To further validate the ranges of frequencies where the control is effective, an expression that yields the critical frequency was derived by assuming the steady-state response of the undamped controlled system for the conditions of partial or full saturation. This closed form expression is given by

$$\frac{\omega_c}{\omega_n} = \sqrt{1 \pm \frac{\alpha c'_{\mathrm{limit}}}{A d^3 (1 + 3\phi) K_t}}, \tag{19}$$

where ω_c is the critical frequency, c'_{limit} the operational capacity of the electromagnet, ϕ the ratio of the amplitude of the desired motion A over the initial distance d, K_t the stiffness coefficient of the EOM and α the magnetic model constant introduced in Section 3.2. The complete derivation of Eq. (19) is presented in the Appendix B.1.

In Fig. 10(c), the effective initial distances were plotted against different desired frequencies of motion in order to highlight the area where the control is effective and the actuator is not saturated. It should be noted that, in this figure, the saturated area refers to full capacity regardless the respective SP. The aforementioned ranges of effective control as well as the non-proportionality with respect to the initial distance are validated. Moreover, for frequencies around ω_n, the control appears to be effective regardless of the choice of initial distance of the magnets. Another interesting point is the prediction of partial saturation for $d = 50$ mm and frequency ratios ω/ω_n lower than 0.5.

In terms of the force exerted by the electromagnet, Fig. 10(d) presents the amplitude range of the force solely for the controllable cases of prescribed desire excitation depending on the initial distance d. The attracting (maximum amplitude) and the repulsive (minimum amplitude) forces are also, to a large extent, symmetric around the mean value of the force, which corresponded to 0 mN.

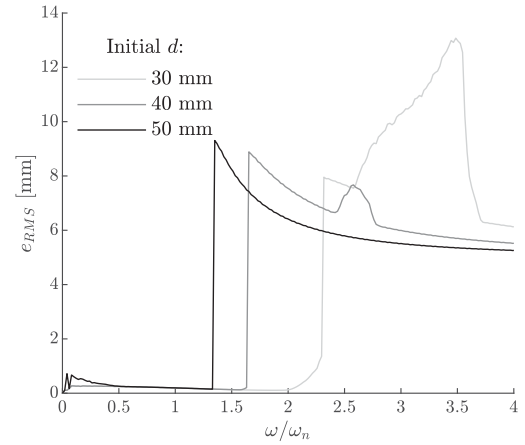

(a) Error e_{RMS} for $A = 5\,\text{mm}$

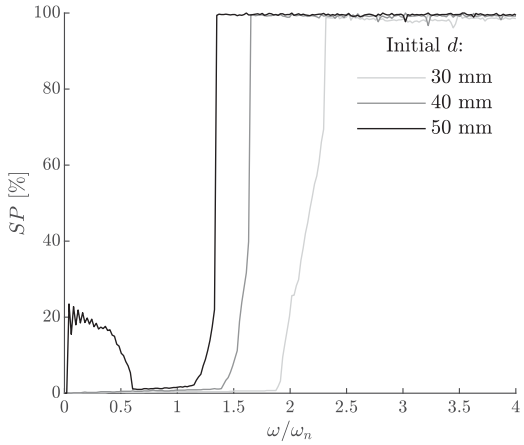

(b) Total saturation $SP(\%)$ for $A = 5\,\text{mm}$

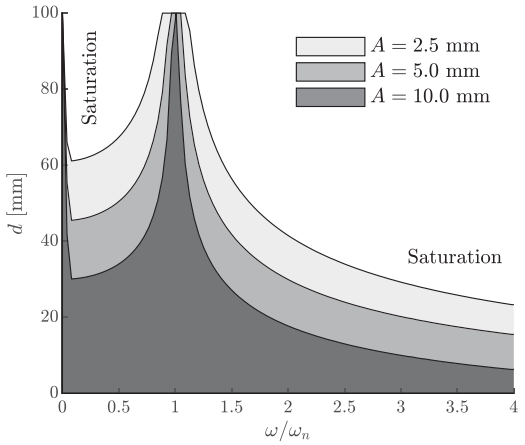

(c) Frequency-controllability curves for different desired amplitude A

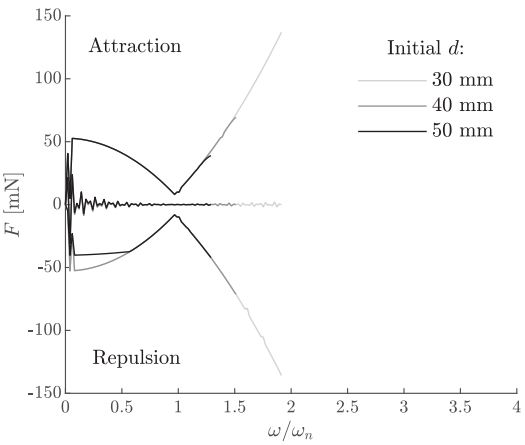

(d) Effective control actuation force F amplitude range for $A = 5\,\text{mm}$

Fig. 10. Control efficiency metrics for each frequency of the desired motion.

As anticipated, the capacity of the electromagnet's force depends on the distance between the EM and the mass of the pendulum, while the forcing amplitudes are not proportional to the separation distance. Furthermore, for certain low or below resonance frequencies ($\omega/\omega_n \leq 1.30$) where the error is insignificant, the control can be executed satisfactory regardless of the separation between the magnets. More specifically, a local minimum of the absolute electromagnetic force is observed at the natural frequency of the uncontrolled system for all different initial separation distances. This observation signifies that the controller is required to apply less force to accomplish the same amplitude of vibration, exploiting the system's resonance.

The highest absolute value of the interaction force is observed for the ratio $\omega/\omega_n = 1.90$ for $d = 30\,\text{mm}$ and is approximately equal to 137 mN. This value corresponds to the unsaturated (effective) control of a simple mass of $\approx 1\,\text{kg}$ or weight of 10 N. Assuming an equal unit of force per unit weight, the ratio of force per weight is $0.137\,\text{N/kg}$. A typical monopile in the offshore wind park *Prinses Amalia* (Netherlands) has a diameter of 4 m and a total mass of 320 t or weight of 3200 kN [30]. A crude estimation of the maximum forcing amplitude for control would be $0.137\,\text{N/kg} \cdot 320 \times 10^3\,\text{kg} = 44\,\text{kN}$. This value is comparable to (or even lower than) the force exerted by active tugger lines controlling the installation of OWT blades with a mass of approximately 18 t as derived in [4].

5.2. Disturbance rejection

Disturbance rejection refers to motion compensation that aims to eliminate the suspended mass' response to external excitation of the system, thus keeping mass M at a fixed position. This control problem is the inverse case of the motion control presented previously. In this section, the pivot point is excited by a prescribed harmonic motion, $h(t) = A\sin(\omega t)$, while the desired position for the payload is constant and equal to $\xi(t) = 0$. A set of constant coefficients for the gains K_p and K_d was selected, which were chosen

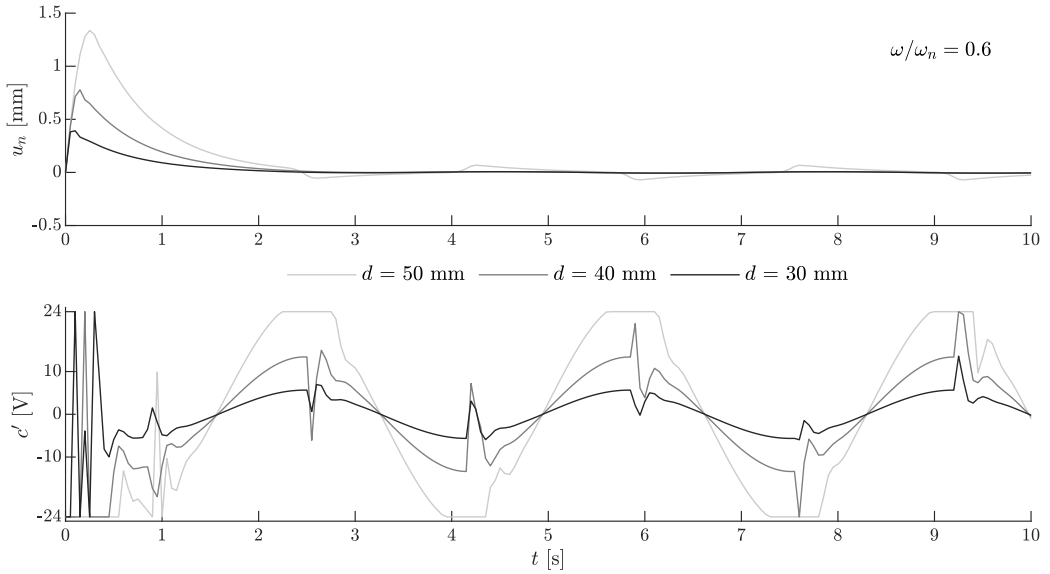

Fig. 11. Displacement u_n (upper) and control output c' (lower) time series of the controlled motion for a harmonic excitation with $A = 5\,\text{mm}$ and desired position $\xi = 0$ for different initial separation distances d.

heuristically by means of trial and error to demonstrate good level of control. The gains of PD control are equal to $K_p = 5000\,\text{N/m}$ and $K_d = 3000\,\text{Ns/m}$ respectively.

For a fixed desired position, $\xi = 0$, the time traces of the controlled motion as well as the respective control output are presented in Fig. 11 for an exemplary case of excitation with amplitude $A = 5\,\text{mm}$ and frequency ratio $\omega/\omega_n = 0.6$ for three initial distances d. Overall, the controller succeeds in attenuating the externally-imposed motion caused by the pivot point and maintain the desired position regardless the excitation frequency. However, during the transient response a large error is observed. As a result, the actuator operates at its limits in order to mitigate the motion. It is noted that the greater the initial distance, the longer the duration of and the higher the initial overshoot in the transient. Nevertheless, this part of the response is, from a broader perspective, short in duration (in the order of few seconds). In the steady-state, a small fluctuation of the error is observed, while the level of saturation depends on the initial distance.

Fig. 12(a) illustrate the maximum error of the overshoot during the transient response (e_{trans}) and after the steady-state response is reached (e_{SS}) for different initial distances d. An almost linear relation is observed between the e_{trans} and the frequency ratio ω/ω_n, with the slope being more steep as the distance of the two magnets increases. Since the most significant deviations occur during the transient, an upper limit of acceptable maximum e_{trans} should be set to serves as an additional efficiency condition next to the critical initial distance d_c. In contrast to the transient, the error during the steady-state response appears to be less significant with one order of magnitude difference between e_{SS} and e_{trans}.

The total saturation SP against different pivot excitation frequencies is given by Fig. 12(b). As expected $d = 50\,\text{mm}$ resulted in the greatest levels of saturation, while for the highest ω/ω_n ratios the controller saturated fully. Moreover, as presented also in the previous control case, the level of saturation of the controller is strongly related to error during the steady-state response. The greatest values of e_{SS} for $d = 50\,\text{mm}$ occur when the controller reaches its limits. An interesting point can be made for the performance of the controller for smaller d, where there is a constant low SP percentage present throughout the rage of the excitation frequencies. These low values correspond to the saturation present during the transient for the case of pivot excitation with amplitude $A = 5\,\text{mm}$.

In Appendix B.2, an expression was derived for the critical frequency ω_c for the steady-state controlled response of the system,

$$\frac{\omega_c}{\omega_n} = \sqrt{\frac{\frac{c_{\text{limit}^{\pm}}}{\gamma A K_t} + 1 - \frac{\xi}{A}}{1 + \frac{B}{M_t}}}, \tag{20}$$

where ω_c is the critical frequency, $c_{\text{limit}^{\pm}}$ the operational capacity of the electromagnet, A is amplitude of the desired motion, ξ the fixed desired position and d the initial distance. The stiffness and mass coefficient of the EOM is given by K_t and M_t respectively, while $B = -\left(M + \frac{m}{2}\right)$.

It should be noted that $1 + B/M_t$ is always negative because $B < 0$. Thus, a physically-admissible critical frequency $(\omega_c > 0)$ can only exist when:

$$\frac{c_{\text{limit}^{\pm}}}{\gamma A K_t} + 1 - \frac{\xi}{A} < 0 \longrightarrow c_{\text{limit}^{\pm}} < \frac{(d-\xi)^3}{\alpha} K_t(\xi - A). \tag{21}$$

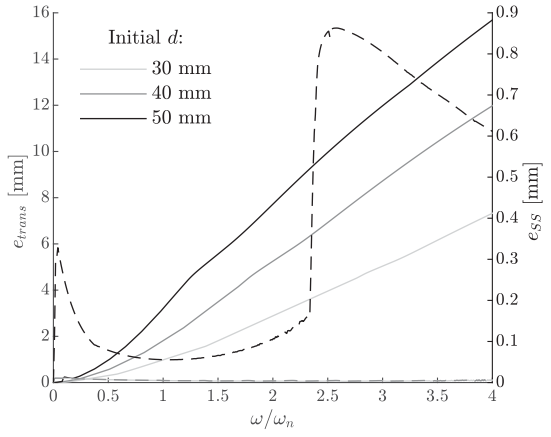

(a) e_{trans} (solid) and e_{SS} (dashed) for $A = 5\,\text{mm}$

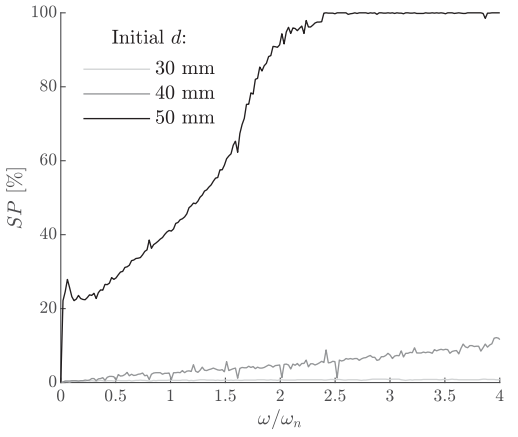

(b) Total saturation $SP(\%)$ for $A = 5\,\text{mm}$

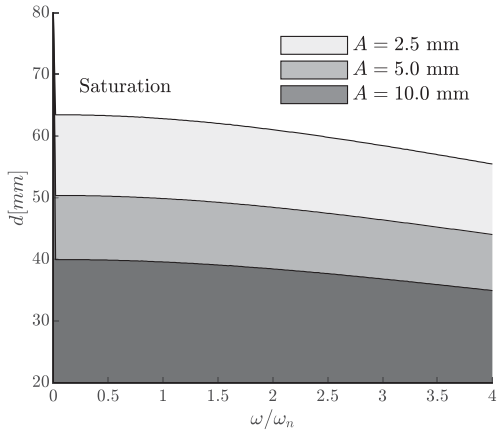

(c) Frequency-controllability curves for different excitation amplitude A (steady-state response)

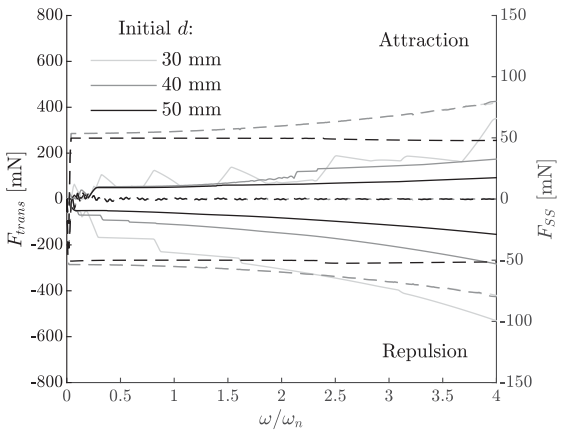

(d) Force range for the transient F_{trans} (solid) and steady-state F_{SS} (dashed) for $A = 5\,\text{mm}$

Fig. 12. Control efficiency metrics for each frequency of the desired motion.

For the special case where the desired position is $\xi = 0$, a condition can be obtained for the critical initial distance d,

$$d < \sqrt[3]{\frac{\alpha \left\| c_{\text{limit}^-} \right\|}{K_t A}} = d_c, \tag{22}$$

where $\left\| c_{\text{limit}^-} \right\|$ signifies the absolute value of the physical limit of the electromagnet. Eq. (22) can be graphically presented in Fig. 12(c) for different excitation amplitudes and frequencies.

By calculating d_c, one practically defines the optimum value for d for the static case of $\omega = 0$ rad/s and the maximum initial distance between the magnets without saturation. This critical distance could serve as a conservative criterion for high controllability (low error in the steady-state response and no saturation). Any initial distance value higher than d_c would result in a degree of saturation for the controller. Fig. 12(c) shows that the control is effective for an extensive range of excitation frequencies, in which the determining parameter is the initial distance. More specifically, for lower frequencies this critical distance is almost constant or exhibits a small reduction of the order of approximately 5 mm. This figure can serve as indicator for a proper choice of d for successful control depending on the amplitude of the pivot motion. For instance, for the case of amplitude $A = 5\,\text{mm}$ and $\omega/\omega_n = 0.6$ presented in Fig. 11, the control is successful (without saturation and no significant error) for $d < 50\,\text{mm}$ during the steady-state, which confirms the validity of the respective controllability curve in Fig. 12(c). However, there is a small tolerance for the critical value, where the control of the system can still be efficient (low error) despite being fully saturated, if one considers the response to $d = 50\,\text{mm}$ in Fig. 11. Thus, the prediction of Eq. (22) is rather conservative, as expected with respect to the assumptions made (i.e. absence of damping and EM self-inductance).

The amplitude range of the force for the transient (F_{trans}, solid lines) and the steady-state (F_{SS}, dashed lines) controlled response is demonstrated in Fig. 12(d) for the different initial distances d. F_{SS} exhibits the same profile for $d \leq 40\,\text{mm}$ as the control is efficient. For $d = 50\,\text{mm}$, due to full saturation and the low error, the controller reaches a certain constant value for all frequency

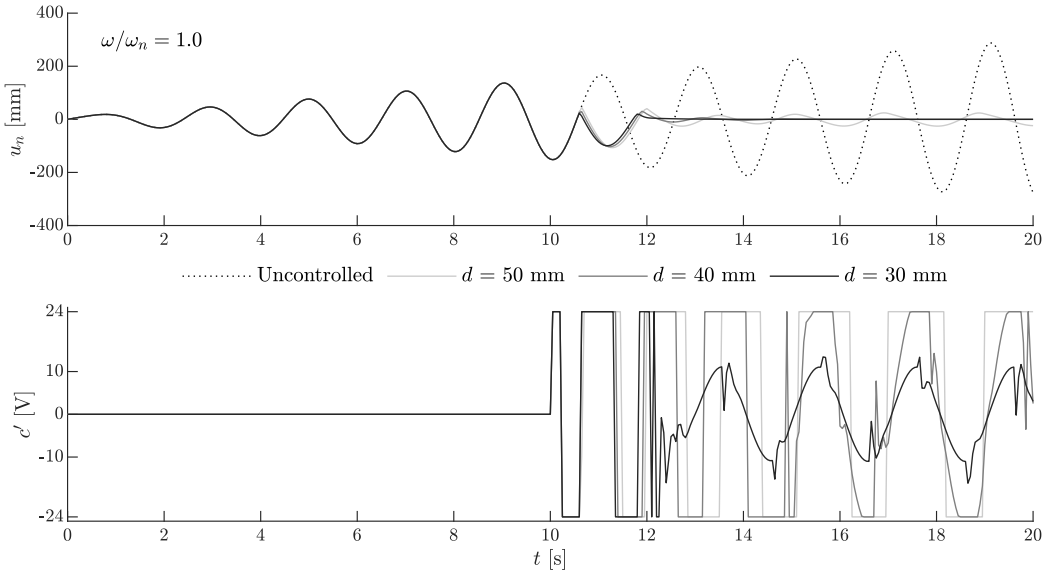

Fig. 13. Comparison of the motion between the controlled and uncontrolled response for different initial distances d and a harmonic excitation amplitude $A = 10\,\text{mm}$.

ratios. Similar behaviour is observed for the force range during the transient response for $d \geq 40\,\text{mm}$. For $d = 30\,\text{mm}$, the profile is less smooth and symmetric around the horizontal axis. It appears that the controller reaches higher force amplitudes in the repulsion regime, which can be explained by the coupling of high e_{trans} and small initial d that results in an even smaller separation $s = d - u_n$ between the two magnets, leading to instability.

The highest absolute value of the interaction force is obtained for the ratio $\omega/\omega_n = 4$ and is approximately equal to 530 mN and 80 mN for F_{trans} and F_{SS} respectively. This order of magnitude corresponds to the unsaturated disturbance control of a simple mass of $\approx 1\,\text{kg}$ or weight of 10 N. For a typical monopile of total mass of 320 t or weight of 3200 kN, the maximum forcing amplitude would amount to 170 kN during the transient and 26 kN for the steady-state response. In this mode of control, the force exerted is higher than when a desired motion was imposed. However, the control is able to attenuate the external perturbation of a larger range of frequencies with success, offering greater controllability. Even for these high forcing amplitudes, the control force over the weight of the object remains low, namely approximately 5%.

Fig. 13 compares the controlled and uncontrolled response of the system to assess the overall efficiency of the motion compensation technique. The control is activated with a 10 sec delay so as to underline the swift response of the control. The uncontrolled response corresponds to the motion of the system due to the applied pivot point excitation in absence of an electromagnet. Overall, it is evident that significant motion mitigation is achieved even for this high value of excitation amplitude ($A = 10\,\text{mm}$). Despite the fact that the system is excited with its natural frequency, the controller is able to prevent the system from exhibiting resonance. More specifically, the controller suppresses instability for $d < 40\,\text{mm}$ as predicted by Fig. 12(c), while it is established that this criterion is rather conservative as the disturbance rejection is effective even for $d = 40\,\text{mm}$ despite the saturation.

5.3. Disturbance rejection for a multiple-frequency pivot excitation

Now, a more realistic signal is prescribed as external excitation for the pivot point $h(t)$ of the pendulum. This signal was obtained from a simulation of a full-scale installation of an OWT tower operated by a semi-submersible vessel (*Prometheus*, [31]) with an input sea state generated by a JONSWAP spectrum with significant wave height $H_s = 3\,\text{m}$ and a peak period $T_p = 8\,\text{s}$. More specifically, the full-scale time response displacement signal $h_{fs}(t)$ of a floating vessel offshore crane tip was scaled in terms of amplitude and time in accordance with the geometry of the experimental set-up by means of Froude scaling. The time series and frequency content of the signals are shown in Fig. 14. The characteristics of the two systems (full-scale and lab-scale) are presented in Table 2. For the full-scale set-up, the dimensions of a typical offshore crane are used.

The scaling factor λ_c is defined as the ratio between a typical length in the full-scale and the experimental set-up. Here, this length is the distance between the deck and the sheave in the top of the crane. Then, the motion h_{fs} and the time t_f of the full-scale data is scaled as

$$h_{sc} = \lambda_c \cdot h_{fs} \quad \text{and} \quad t = \sqrt{\lambda_c} \cdot t_f, \tag{23}$$

ensuring that the imposed signal in the simulations has the same frequency content relative to the natural frequency as the full-scale signal. In order to demonstrate the control through simulations, a one-minute fragment of the scaled displacement time series is

Table 2
Dimension comparison between the experimental and full-scale set-up.

Parameters	Full-scale	Lab-scale	Ratio
Crane length [m]	$L_{c,f} = 140$	$L_{c,s} = 1.22$	$\lambda_c = 8.7 \times 10^{-3}$
Pendulum arm [m]	$L_{p,f} = 80$	$L_{p,s} = 1.04$	–
Natural frequency [Hz]	$f_{n,f} = 0.056$	$f_{n,s} = 0.489$	–

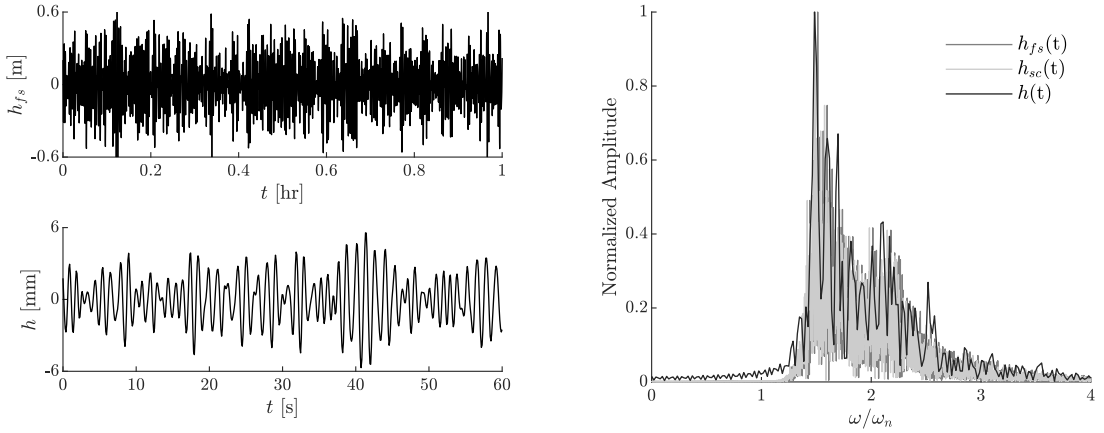

(a) Time series of the crane tip displacement for the full-scale (h_{fs}) and scaled signal (h)

(b) Frequency response of the full-scale (h_{fs}) and scaled signals (h_{sc} & h)

Fig. 14. Amplitude time series and frequency content of the pivot point excitation signal input.

deduced and is shown in Fig. 14(a) as $h(t)$. Fig. 14(b) presents the frequency contents of the three main signals, namely the full-scale crane-tip $h_{fs}(t)$, the scaled counterpart $h_{sc}(t)$ and the final crane-tip displacement $h(t)$ imported as excitation to the model. The frequency scale is normalized with the natural frequency of the two set-ups respectively. Small discrepancies are observed when comparing the full-scale and scaled signals due to the simplification assumptions made in calculating the natural frequency of the full-scale dynamical system $f_{n,f}$. The offshore crane-payload system is assumed to be equivalent to a simple point mass pendulum with a mass-less inflexible arm. In all spectra, multiple frequency components are present and the overall energy corresponds to ratios $\omega/\omega_n > 1$.

Fig. 15 presents the relevant time traces of the controlled motion for different separation distances. For the displacement u_n, an excellent level of attenuation of motion is achieved for all d. The main differences pertain to the transient part of the response, namely the amplitude of the error and the duration of the transient. Reducing the distance results in a lower error and a shorter transient response, which is in line with the previous results. Moreover, the total level of saturation of the control output c decreases for $d < 50$ mm.

However, to assess the total efficiency of the control and to connect it to real-life operations and technical capacities, the consumed power needs to be examined. There are two main power components to be considered:

1. the power required to control the payload which is associated with the work done by the actuation force (P_F) and
2. the electrical power consumed to enable the control actuation (P_I). To define the latter power, the resistance of the feeding electrical circuit R is needed.

Since this parameter of the system is unspecified in the present set-up, $P_I \cdot R$ ($= J \cdot c'$, where c' and J are the voltage input and output of the actuator respectively) is examined in Fig. 15 instead. As intuitively expected, the electrical power ($P_I \cdot R$) consumed by the controller becomes greater with the initial distance. When the control is efficient, during steady-state, the effort of the actuation (P_F) is the same regardless the separation. Differences are highlighted during the transient, where the response for $d = 30$ mm exhibits the highest work required to achieve low error.

By comparing all the time series reported in Fig. 15, the most effective control case for this multiple frequency signal is the distance $d = 40$ mm in terms of the error and actuation power and the distance $d = 30$ mm in terms of saturation and electrical power. This discrepancy underlines the importance of consciously selecting the distance not only aiming at less energy consumption but also ensuring the stability and safety of the operation, as the nature of the interaction becomes highly non-linear as the distance decreases.

6. Conclusion

A proof of concept of a new contactless position control technique for OWT installations is presented. In order to achieve this, an equivalent dynamical system is studied, namely a magnetic pendulum subjected to electromagnetic forcing and pivot point

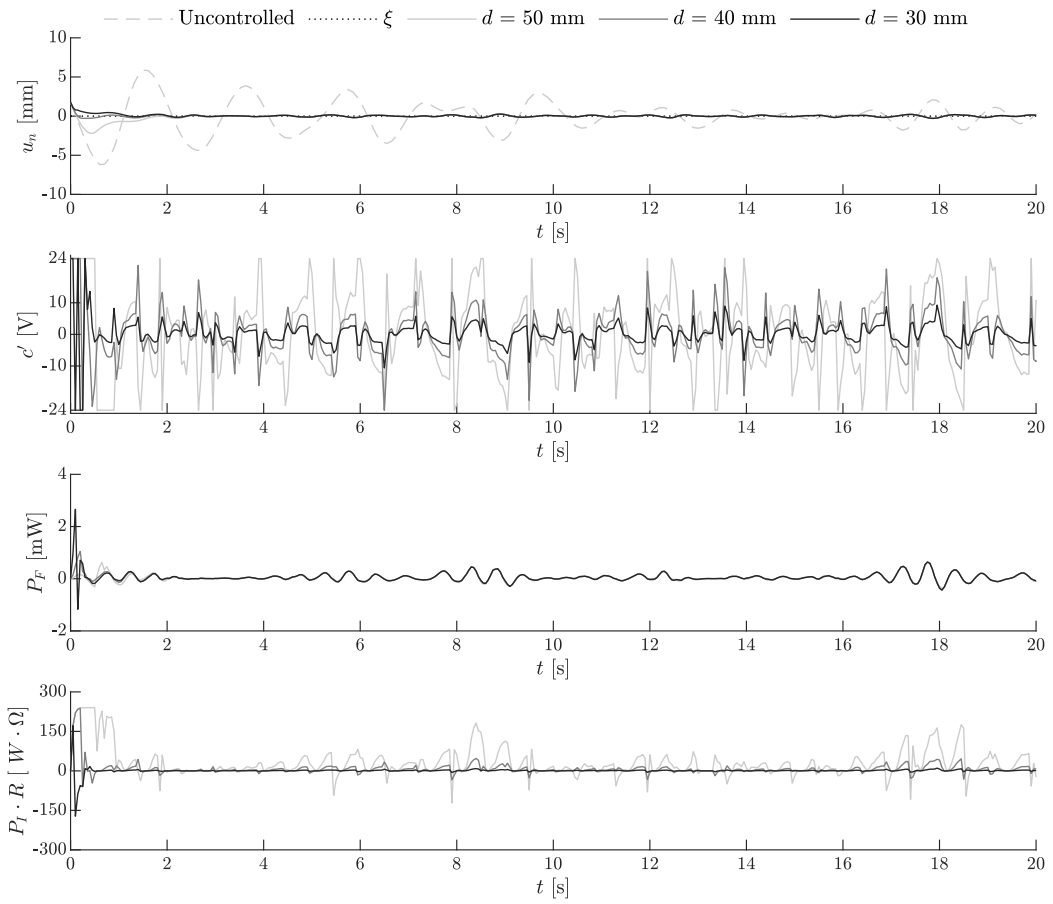

Fig. 15. Controlled response for disturbance rejection of a multiple frequency excitation: Times series of the displacement u_n, control output c, control actuation power P_F and electrical power consumed by actuation times the resistance $P_I \cdot R$.

excitation. A mathematical model of the system is developed and simulations are validated and calibrated against experiments on lab scale. For the controlled vibrations, a modified PD controller is employed to enforce a certain position or motion to the load through regulating the intensity and polarity of an electromagnet.

The technique is successful for two different control modes: desired motion of the payload with a fixed pivot and fixed global position with moving pivot point. Two important control parameters are identified: the saturation of the controller and the separation distance of the two magnets. It is noted that the swifter the transitions between the two polarities during the control, the longer the time where the electromagnet operates at its full capacity, leading to an inferior response. The relative distance between the magnets plays an equally crucial role. When the magnets operate in closer proximity, the performance of the control is significantly improved (lower error and less saturation). Controllability curves are derived numerically as indication of areas of efficient control. These curves serve as nomographs, through which the optimum distance between the magnets can be deduced for different combinations of excitation (external excitation or desired motion). Resonance is exploited by the controller when a desired harmonic motion is imposed, while this behaviour is successfully subdued when the controller aims at a fixed position. For the latter control mode, transient response is of great importance for the overall efficiency of the control of the system as it leads to large errors and high saturation levels, which attenuate when steady-state is reached. It is important, therefore, to set an additional criterion for the maximum acceptable error during transient. The power required can be also indicative of the optimum choice of initial separation distance for the magnets: with the power of the control actuation force being in favour of an intermediate distance, while the electrical power suggesting smaller distances as the least energy demanding. In terms of force amplitude exerted by the actuator, the estimated order of magnitude is comparable to an active tugger line control system, but with a crucial difference: both repulsive and attracting forces are possible, thus allowing for more control authority.

In short, the contactless control technique that exploits magnetic interaction succeeds in both maintaining a desired fixed position with a moving pivot point and imposing a desired harmonic motion to a suspended mass. The findings of this work underline the potential for the further advancement of this contactless motion control technique, and the eventual design of a more intricate multi-degree motion control algorithm for offshore applications.

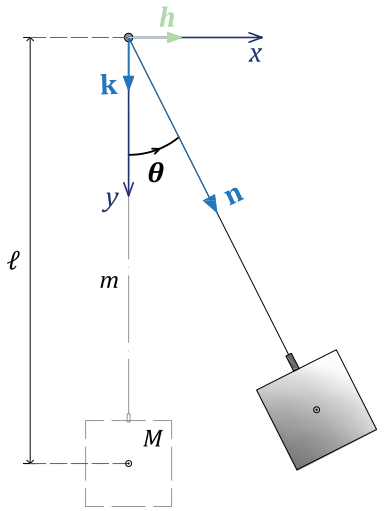

Fig. A1. Schematic diagram of the dynamical system.

CRediT authorship contribution statement

Panagiota Atzampou: Conceptualization, Data curation, Investigation, Methodology, Validation, Visualization, Writing – original draft, Writing – review & editing, Formal analysis. **Peter C. Meijers:** Conceptualization, Investigation, Methodology, Supervision, Validation, Writing – review & editing. **Apostolos Tsouvalas:** Conceptualization, Funding acquisition, Supervision, Writing – review & editing. **Andrei V. Metrikine:** Conceptualization, Funding acquisition, Project administration, Supervision, Writing – review & editing.

Declaration of competing interest

The authors declare that they have no known competing financial interests or personal relationships that could have appeared to influence the work reported in this paper.

Data availability

Data will be made available on request.

Acknowledgements

The authors gratefully acknowledge the contribution of David Fidalgo Domingos, PhD candidate in Delft Center for Systems and Control for providing them with the realistic multiple-frequency crane tip displacement signal shown in the present work. Credits should also be given to Fred Schilperoort, Kees van Beek, Jaap Elstgeest and Peter de Vries from the Stevin II laboratory of the Delft University of Technology for their support during the experimental tests. Moreover, this contribution belongs to the work plan of the DOT6000-FOX project subsidized by the Rijksdienst voor Ondernemend Nederland (Project ID: TEHE119004) and shared between the partners: Delft University of Technology, Delft Offshore Turbine B.V. (DOT) and Heerema Marine Contractors (HMC).

Appendix A. Derivation of equations of motion

The equation of motion that describes the free in-plane oscillation of a point mass pendulum in polar coordinates is given by

$$M\ell^2\ddot{\theta} + Mg\ell\sin\theta = 0, \tag{A.1}$$

where M and ℓ represent the mass and the arm length of the pendulum, while θ is the unknown state variable of the system, namely the angle of rotation of the hinge. The gravitational acceleration equals to $g = 9.81\,\mathrm{m/s^2}$. For the dynamical system studied in this paper, the mass of the rod of the pendulum is not neglected and its contribution is included in the governing equation. In Fig. A1, the important parameters of the pendulum are presented.

In order to describe the motion of the pendulum, the coordinates of the position of the two components are calculated and are given as

$$\vec{P}_n(t) = \vec{P}(t) + \vec{H}(t) = \begin{pmatrix} \ell\sin\theta \\ \ell\cos\theta \end{pmatrix} + \begin{pmatrix} h(t) \\ 0 \end{pmatrix}, \tag{A.2a}$$

$$\vec{P}_{rn}(t) = \vec{P}_r(t) + \vec{H}(t) = \begin{pmatrix} \mathbf{n}\sin\theta \\ \mathbf{n}\cos\theta \end{pmatrix} + \begin{pmatrix} h(t) \\ 0 \end{pmatrix}, \tag{A.2b}$$

where $\vec{P}(t)$ and $\vec{P}_r(t)$ are the position vectors of the system masses and $\mathbf{n}$ refers to a vector extending from the pivot point to the total length of the pendulum arm. The kinetic (K) and potential (P) energy of the dynamical system are calculated to be equal to

$$K = \frac{1}{2} M \|\vec{P}_n(t)\|^2 + \frac{1}{2}\frac{m}{\ell}\int_0^{\ell} \|\vec{P}_{rn}(t)\|^2 \, \mathrm{d}\mathbf{n}, \tag{A.3a}$$

$$P = Mg\left(\ell - \vec{k}\vec{P}_n(t)\right) + \frac{m}{\ell} g\left(\int_0^{\ell}\left(\ell - \vec{k}\,\vec{P}_{rn}(t)\right)\mathrm{d}\mathbf{n}\right), \tag{A.3b}$$

where $\vec{k}$ represents the unit vector of the vertical direction (y-axis). For the derivation of the equation of motion, the Lagrangian ($\mathcal{L}$) was formulated and it was equal to

$$\frac{d}{dt}\left(\frac{\partial \mathcal{L}}{\partial \dot{\theta}}\right) - \frac{\partial \mathcal{L}}{\partial \theta} = 0 \text{ with } \mathcal{L} = K - P, \tag{A.4}$$

$$\left(M + \frac{m}{3}\right)\ell^2\ddot{\theta} + \left(M + \frac{m}{2}\right) g\ell \sin(\theta) = -\left(M + \frac{m}{2}\right)\ell\ddot{h}\cos(\theta), \tag{A.5}$$

Appendix B. Derivation of the critical frequency

When a harmonic desired motion is prescribed to the controlled system, the controller reaches the limiting value for a certain combination of motion amplitude A, motion frequency ω and initial distance d. To derive an expression for the saturation values, the steady-state response of the system is analysed. If one assumes that the delay of the electromagnet and the non-linear Coulomb damping are negligible in the steady-state regime, the resulting linear equation of motion of the controlled pendulum reads:

$$\left(M + \frac{m}{3}\right)\ddot{u} + \left(M + \frac{m}{2}\right)\frac{g}{\ell}u = -\left(M + \frac{m}{2}\right)\ddot{h} + K_p(\xi - h - u) + K_d(\dot{\xi} - \dot{h} - \dot{u}), \tag{B.1}$$

where ξ is the desired motion of the mass, h is the pivot point motion and u is the response of the pendulum. Eq. (B.1) is a linear ordinary differential equation, which can be rewritten more concisely as

$$M_t\ddot{u} + K_t u = B\ddot{h} + K_p(\xi - h - u) + K_d(\dot{\xi} - \dot{h} - \dot{u}). \tag{B.2}$$

With this expression, the modified control output is given by the following expression,

$$c' = \gamma\left[K_p(\xi - h - u) + K_d(\dot{\xi} - \dot{h} - \dot{u})\right] = \gamma\left[M_t\ddot{u} + K_t u - B\ddot{h}\right], \tag{B.3}$$

with $\gamma = (d - u_n)^3/\alpha$. The two distinct cases of control studied in this work can result to two different expressions for the critical frequency ω_c:

B.1. Motion control

In this control scenario, the pivot point is considered fixed ($h(t) = 0$) and its objective is to impose a desired motion on the mass, $\xi(t)$. Eq. (B.3) is given by

$$c' = \gamma\left(K_p(\xi - u) + K_d(\dot{\xi} - \dot{u})\right). \tag{B.4}$$

The control is effective as long as it remains within the controller limits and not saturate. The first condition ensures that the motion is approximately equal to the desired motion, namely $u \approx \xi = A\sin(\omega t)$ where A is the amplitude and ω is the frequency of the desired response.

$$c' = \frac{Ad^3\left(K_t - \omega^2 M_t\right)}{\alpha}(1 - \phi\sin(\omega t))^3\sin(\omega t), \tag{B.5}$$

in which $\phi = A/d$. To check the frequency at which the controller is (partially) saturated, one must check when the amplitude of the control signal is above or below the limit. The second condition pertains to the limit case in which the control output is approximately equal to the physical limit $c_{\text{limit}^{\pm}}$. Hence, the following expression holds at the critical frequency ω_c:

$$c_{\text{limit}^{\pm}} = \frac{Ad^3(K_t - \omega^2 M_t)Q}{\alpha} \tag{B.6}$$

with $Q = 1 - 3\frac{A}{d} + 3\frac{A^2}{d^2} - 3\frac{A^3}{d^3}$.

Solving for ω_c gives the following closed form expression:

$$\frac{\omega_c}{\omega_n} = \sqrt{\frac{\alpha c_{\text{limit}^{\pm}}}{AK_t d^3 Q} + 1} \tag{B.7}$$

Note that only the real valued solutions of this expression have physical significance.

B.2. Disturbance rejection

In the following, the motion of the pivot point is prescribed and equals to a harmonic sinusoidal motion with amplitude A and frequency ω, namely $h = A\sin(\omega t)$.

The desired motion ξ is not a function of time but rather a constant desired position for the mass of the pendulum in the global reference frame. Hence, higher order derivatives of the desired motion are zero. Moreover, in order to define a criterion for effective control, two conditions need to be met. First, for the error of the control, $e \approx 0$ should apply, and, consequently, the steady-state response of the pendulum can be approximated as $u \approx \xi - h$. After substitution of the first condition to Eq. (B.3) and further simplifications one obtains

$$c' = \gamma\left[M_t\omega^2 A - K_t A + B\omega^2 A\right]\sin(\omega t) + \gamma K_t \xi, \tag{B.8}$$

with $\gamma = (d-\xi)^3/\alpha$. Second, there is a condition for effective control that pertains to the saturation and the limits of the control signal. Saturation occurs when the amplitude of the c' is equal to $c_{\text{limit}^{\pm}}$. As the amplitude of a pure sinusoidal signal is given by the factor in front of the sin function, this condition, if applied to Eq. (B.8), yields

$$c_{\text{limit}^{\pm}} = \frac{(d-\xi)^3}{\alpha}\left[M_t\omega_c^2 A - K_t A + B\omega_c^2 A + K_t\xi\right], \tag{B.9}$$

where ω_c refers to the critical frequency above which the controller saturates partially or fully. Solving for the ratio of the critical frequency over the natural frequency of the system (ω_c/ω_n) gives the following closed form expression:

$$\frac{\omega_c}{\omega_n} = \sqrt{\frac{\frac{c_{\text{limit}^{\pm}}}{\gamma A K_t} + 1 - \frac{\xi}{A}}{1 + \frac{B}{M_t}}}. \tag{B.10}$$

References

[1] Wind energy in Europe: 2021 Statistics and the outlook for 2022–2026 | WindEurope, URL https://windeurope.org/intelligence-platform/product/wind-energy-in-europe-2021-statistics-and-the-outlook-for-2022-2026/.

[2] L. Li, Dynamic Analysis of the Installation of Monopiles for Offshore Wind Turbines (Ph.D. thesis), Norwegian University of Science and Technology, 2016.

[3] Z. Jiang, Installation of offshore wind turbines: A technical review, Renew. Sustain. Energy Rev. 139 (2021) 110576, http://dx.doi.org/10.1016/J.RSER.2020.110576.

[4] Z. Ren, Z. Jiang, Z. Gao, R. Skjetne, Active tugger line force control for single blade installation, Wind Energy 21 (2018) 1344–1358, http://dx.doi.org/10.1002/WE.2258.

[5] S. Wang, Y. Sun, H. Chen, J. Du, Dynamic modelling and analysis of 3-axis motion compensated offshore cranes, Ships Offshore Struct. 13 (3) (2018) 265–272, http://dx.doi.org/10.1080/17445302.2017.1360981.

[6] W. O'Connor, H. Habibi, Gantry crane control of a double-pendulum, distributed-mass load, using mechanical wave concepts, Mech. Sci. 4 (2013) 251–261, http://dx.doi.org/10.5194/MS-4-251-2013.

[7] D.H. Lee, T.W. Kim, S.W. Ji, Y.B. Kim, A study on load position control and vibration attenuation in crane operation using sub-actuator, Meas. Control 52 (2019) 794–803, http://dx.doi.org/10.1177/0020294019847703.

[8] J. Neupert, T. Mahl, B. Haessig, O. Sawodny, K. Schneider, A heave compensation approach for offshore cranes, Proc. Am. Control Conf. (2008) 538–543, http://dx.doi.org/10.1109/ACC.2008.4586547.

[9] L.B. Zhang, A. Abdelkefi, H.L. Dai, R. Naseer, L. Wang, Design and experimental analysis of broadband energy harvesting from vortex-induced vibrations, J. Sound Vib. 408 (2017) 210–219, http://dx.doi.org/10.1016/J.JSV.2017.07.029.

[10] T.G. Larsen, Z. Zhang, J. Høgsberg, Vibration damping of an offshore wind turbine by optimally calibrated pendulum absorber with shunted electromagnetic transducer, J. Sound Vib. 505 (2021) 116144.

[11] V.N. Pilipchuk, K. Polczyński, M. Bednarek, J. Awrejcewicz, Guidance of the resonance energy flow in the mechanism of coupled magnetic pendulums, Mech. Mach. Theory 176 (2022) 105019, http://dx.doi.org/10.1016/j.mechmachtheory.2022.105019.

[12] A.N. Kadjie, P. Woafo, Effects of springs on a pendulum electromechanical energy harvester, Theor. Appl. Mech. Lett. 4 (2014) 063001, http://dx.doi.org/10.1063/2.1406301.

[13] R. Kumar, S. Gupta, S.F. Ali, Energy harvesting from chaos in base excited double pendulum, Mech. Syst. Signal Process. 124 (2019) 49–64, http://dx.doi.org/10.1016/J.YMSSP.2019.01.037.

[14] M. Wojna, A. Wijata, G. Wasilewski, J. Awrejcewicz, Numerical and experimental study of a double physical pendulum with magnetic interaction, J. Sound Vib. 430 (2018) 214–230, http://dx.doi.org/10.1016/J.JSV.2018.05.032.

[15] A. Wijata, K. Polczyński, J. Awrejcewicz, Theoretical and numerical analysis of regular one-side oscillations in a single pendulum system driven by a magnetic field, Mech. Syst. Signal Process. 150 (2021) 107229, http://dx.doi.org/10.1016/J.YMSSP.2020.107229.

[16] S. Skurativskyi, K. Polczyński, M. Wojna, J. Awrejcewicz, Quantifying periodic, multi-periodic, hidden and unstable regimes of a magnetic pendulum via semi-analytical, numerical and experimental methods, J. Sound Vib. 524 (2022) 116710, http://dx.doi.org/10.1016/j.jsv.2021.116710.

[17] A. Siahmakoun, V.A. French, J. Patterson, Nonlinear dynamics of a sinusoidally driven pendulum in a repulsive magnetic field, Amer. J. Phys. 65 (1998) 393, http://dx.doi.org/10.1119/1.18546, URL https://aapt.scitation.org/doi/abs/10.1119/1.18546.

[18] K.R. Austin, J.R. Wagner, Development of an electromagnet excited mass-pendulum system modeling and control laboratory experiment - theory and test, in: 2013 European Control Conference, ECC 2013, IEEE Computer Society, 2013, pp. 256–261, http://dx.doi.org/10.23919/ECC.2013.6669112.

[19] N. Ida, Design and control of a magnetic pendulum actuator, in: Proceedings of the International Conference on Optimisation of Electrical and Electronic Equipment, OPTIM, 2012, pp. 439–443, http://dx.doi.org/10.1109/OPTIM.2012.6231898.

[20] A. Fradkov, B. Andrievsky, K. Boykov, Control of the coupled double pendulums system, Mechatronics 15 (10) (2005) 1289–1303, http://dx.doi.org/10.1016/j.mechatronics.2005.03.008.

[21] Y. Kraftmakher, Demonstrations with a magnetically controlled pendulum, Amer. J. Phys. 78 (2010) 532, http://dx.doi.org/10.1119/1.3276412, URL https://aapt.scitation.org/doi/abs/10.1119/1.3276412.

[22] DOB-Academy, FOX Project video - Offshore Campaign, Youtube, 2022, URL https://www.youtube.com/watch?v=BGcLoREJI-c.

[23] G. Torzo, P. Peranzoni, The real pendulum: theory, simulation, experiment, Lat. Am. J. Phys. Educ. Vol (2009) URL https://www.academia.edu/835053/The_real_pendulum_theory_simulation_experiment.

[24] A. Cabboi, J. Woodhouse, Validation of a constitutive law for friction-induced vibration under different wear conditions, Wear 396–397 (2018) 107–125, http://dx.doi.org/10.1016/J.WEAR.2017.08.010.
[25] D.J. Griffiths, Introduction to Electrodynamics, Cambridge University Press, 2017, http://dx.doi.org/10.1017/9781108333511.
[26] M.S. Sarma, Introduction to Electrical Engineering, Oxford University Press, 2001.
[27] K.J. Åström, M.R. M., Feedback Systems: An Introduction for Scientists and Engineers, 2008, URL https://www.researchgate.net/publication/36721090_Feedback_Systems_An_Introduction_for_Scientists_and_Engineers.
[28] H.K. Khalil, Nonlinear Systems, third ed., Pearson, Upper Saddle River, NJ, 2001.
[29] T. Chai, R.R. Draxler, Root mean square error (RMSE) or mean absolute error (MAE), Geosci. Model Dev. Discuss. 7 (1) (2014) 1525–1534.
[30] V. Negro, J.-S. López-Gutiérrez, M.D. Esteban, P. Alberdi, M. Imaz, J.-M. Serraclara, Monopiles in offshore wind: Preliminary estimate of main dimensions, Ocean Eng. 133 (2017) 253–261, http://dx.doi.org/10.1016/j.oceaneng.2017.02.011.
[31] D. Domingos, P. Wellens, J.W. van Wingerden, Prometheus: An open-source SSCV, 4TU.ResearchData (2023) http://dx.doi.org/10.4121/aa0a24fc-b7e2-4e05-b0cb-f1dc2af1c9ac.